Fluorite-type Tm^{3+}:KY_3F_{10}: A promising crystal for watt-level lasers at ~1.9 μm

Mengting Chen,[1,2] Pavel Loiko,[3] Josep Maria Serres,[2] Stefano Veronesi,[4] Mauro Tonelli,[4] Magdalena Aguiló,[2] Francesc Díaz,[2] Sun Yung Choi,[5] Ji Eun Bae,[5] Fabian Rotermund,[5] Shibo Dai,[1] Zhenqiang Chen,[1] Uwe Griebner,[6] Valentin Petrov,[6] and Xavier Mateos[2,*]

[1]*Department of Optoelectronic Engineering, Jinan University, Tianhe District, Guangzhou 510632, China*
[2]*Universitat Rovira i Virgili, Departament Química Física i Inorgànica, Física i Cristal·lografia de Materials i Nanomaterials (FiCMA-FiCNA)-EMaS, Campus Sescelades, E-43007, Tarragona, Spain*
[3]*ITMO University, 49 Kronverkskiy Pr., 197101 St. Petersburg, Russia*
[4]*NEST Istituto Nanoscienze-CNR and Dipartimento di Fisica dell'Università di Pisa, Largo B. Pontecorvo 3, 56127 Pisa, Italy*
[5]*Department of Physics, KAIST, 291 Daehak-ro, Yuseong-gu, 34141 Daejeon, South Korea*
[6]*Max Born Institute for Nonlinear Optics and Short Pulse Spectroscopy, Max-Born-Str. 2a, D-12489 Berlin, Germany*
**Corresponding author, e-mail: xavier.mateos@urv.cat*

ABSTRACT: Tm^{3+}-doped cubic potassium yttrium fluoride, KY_3F_{10}, is a promising laser crystal for efficient watt-level lasers at ~1.9 μm because of the relatively easy crystal growth by the Czochralski method, advantageous thermo-optical properties, high available Tm^{3+} doping levels and very efficient cross-relaxation mechanism. A compact diode-pumped 8 at.% Tm^{3+}:KY_3F_{10} laser generated 1.85 W at 1891 nm with a slope efficiency of 65.2% and a laser threshold of 450 mW. A negative thermal lens was detected in this crystal owing to the negative dn/dT coefficient (-8.9×10^{-6} K^{-1}). Passive Q-switching of the Tm^{3+}:KY_3F_{10} laser by single-walled carbon nanotube saturable absorber was demonstrated yielding 13.2 μJ / 490 ns pulses at a repetition rate of 58 kHz.

Keywords: Fluoride crystals; Thulium ions; Crystal growth; Optical spectroscopy; Thermo-optical properties; Laser operation.

1. Introduction

Fluoride crystals represent an important class of laser host materials for doping with rare-earth ions (RE^{3+}) [1]. As host matrices, they exhibit several advantageous properties as compared to their oxide counterparts, i.e., broad transparency range and typically large bandgap, relatively low refractive index, low phonon energies and attractive thermo-mechanical behavior, in particular, high thermal conductivity. The RE^{3+} ions in fluorides exhibit long lifetimes of the excited states [2]. Moreover, there exist a variety of fluoride crystals with different structures such as cubic (CaF_2 [3,4], SrF_2 [5] or their solid solutions [6]) trigonal (KYF_4 [7]), tetragonal ($LiYF_4$, $LiGdF_4$, $LiLuF_4$ [8]) or even monoclinic (BaY_2F_8 [9, 10]) which may accommodate RE^{3+} ions with high concentrations.

Among the cubic (sp. gr. $Fm\bar{3}m$) fluoride crystals, potassium yttrium fluoride (KY_3F_{10}) has been relatively poorly studied regarding the laser applications [11-13] compared to more widespread calcium fluoride (CaF_2) and its isomorphs. Note that KY_3F_{10} is abbreviated as KYF while it has to be distinguished from other crystals appearing in the $KF–YF_3$ binary system, such as the trigonal KYF_4 [7] or the orthorhombic K_2YF_5 [14]. KY_3F_{10} melts congruently at the temperature of 1020 °C (lower than that for CaF_2), so that it can be grown by the conventional Czochralski (Cz) method [15]. Contrary to CaF_2, this crystal exhibits a single crystallographic site (Y^{3+} one) for RE^{3+} dopants [16] which may be occupied in high concentrations preserving good optical quality of the crystal.

In recent years, there has been an interest for developing novel solid-state gain materials for laser emission in the eye-safe spectral range at ~2 μm [17,18]. Such lasers are of practical importance for medicine, bio- and environmental sensing, range-finding, spectroscopy and further spectral conversion to the mid-IR [19]. Typically, the laser emission at ~2 μm is achieved using thulium (Tm^{3+}) or holmium (Ho^{3+}) ions. For the former case, it relies on the $^3F_4 \rightarrow {}^3H_6$ electronic transition. Tm^{3+} ions can be efficiently pumped by commercial AlGaAs laser diodes emitting at ~0.8 μm (to the $^3H_4$ state) and the corresponding pump quantum efficiency may reach 2 due to the very efficient cross-relaxation (CR) process, $^3H_4 + {}^3H_6 \rightarrow {}^3F_4 + {}^3F_4$ [20]. The Stark splitting of the Tm^{3+} ground-state ($^3H_6$) is typically large leading to a broadband emission while a proper selection of the host material may shift the spectral range of Tm^{3+} laser emission due to the varied crystal-field.

From these considerations, we decided to reconsider the cubic Tm^{3+}:KY_3F_{10} crystal regarding its ability to generate laser emission at ~1.9 μm. We also focused on its feature to tolerate high Tm^{3+} doping levels. Recently, fluoride crystals featuring high Tm^{3+} doping (up to 18 at.%) were studied leading to several interesting results [8,9]. Loiko *et al*. achieved efficient laser operation of a diode-pumped microchip-type 8 at.% Tm^{3+}:$LiYF_4$ laser delivering 3.10 W at 1904 nm with a slope efficiency of 72% [8]. Cornacchia *et al*. demonstrated vibronic laser operation of a 18 at.% Tm^{3+}:BaY_2F_8 laser operating at a wavelength as long as 2030 nm [9]. For Tm^{3+}-doped laser crystals, an increase of the doping concentration is in general desirable because of (i) better pump absorption efficiency, (ii) strong CR for adjacent Tm^{3+} ions leading to the laser slope efficiency well exceeding the Stokes limit, and (iii) typically longer emission wavelengths because of increased reabsorption.

Regarding Tm^{3+}:KY_3F_{10}, room- and low-temperature spectroscopy [11,15], energy transfer in the Yb^{3+}-Tm^{3+} system [21] and diode-pumped laser performance [11] have been reported. Braud *et al*. demonstrated a 5 at.% Tm^{3+}:KY_3F_{10} laser generating 0.27 W at 1846 nm with a slope efficiency of 42.5% [11]. ~2.3 μm laser operation (at the $^3H_4 \rightarrow {}^3H_5$ transition) from a highly-doped 8 at.% Tm^{3+}:KY_3F_{10} crystal was reported [22]. Regarding recent studies of KY_3F_{10}-based materials, the emission properties of RE^{3+}-doped KY_3F_{10} nanocrystals [23-25] and thin-films [26] were studied. Crystallization of RE^{3+}-doped glass-ceramics based on the isostructural KGd_3F_{10} compound was reported [27].

In the present work, we describe the crystal growth, spectroscopic and thermo-optic properties and efficient ~1.9 μm laser operation (at the $^3F_4 \rightarrow {}^3H_6$ transition) of highly-doped 8 at.% Tm^{3+}:KY_3F_{10} crystals, for the first time, to the best of our knowledge. We show that Tm^{3+}:KY_3F_{10} is suitable for watt-level continuous-wave lasers at ~1.9 μm with characteristics being competitive to the well-known cubic Tm^{3+}:CaF_2 crystals.

2. Crystal growth

KY_3F_{10} has appealing characteristics, such as congruent melting, optical isotropy, good thermo-mechanical properties [16] and it can be grown relatively easy. Nevertheless, to obtain excellent optical quality within the entire crystal boule is challenging. To ensure excellent quality in large boule size, the crystal growth was carried out following the description previously patented in [28]. The Tm^{3+}:KY_3F_{10} single crystal was grown in the Physics Department of the National Enterprise for nano-Science and nano-Technology Laboratories, Pisa, Italy. The growth was performed in a home-made Czochralski furnace from an oriented seed using high purity (5N) raw powders. The pulling rate was 1 mm/h and the rotation speed was 5 rpm. The crystal had a Tm^{3+} doping concentration of 8.0 at.% (stoichiometric formula: $K(Y_{0.920}Tm_{0.080})_3F_{10}$), corresponding to an ion density of 12.5×10^{20} at/cm^3. The photograph of the as-grown crystal boule is shown in Fig. 1.

KY_3F_{10} belongs to the cubic crystal class (sp. gr. O^5_h – $Fm\bar{3}m$, No. 225). Its lattice constant amounts to a = 11.554 Å and the number of formula units in the unit-cell is Z = 8 (density: ρ = 4.22 g/cm^3) [16]. The structure of KY_3F_{10} represents a 2×2×2 superstructure of fluorite. The trivalent cations (Y^{3+}) are incorporated into distorted square antiprisms (VIII-fold coordination). The K^+ cations are coordinated tetrahedrally by four inner fluorine atoms; 12 anions are positioned at longer distances. The crystal symmetry makes KY_3F_{10} an attractive material to develop cheap devices in ceramic form.

3. Material characterization

3.1 Spectroscopic properties

Cubic KY_3F_{10} crystals are optically isotropic. Tm^{3+} doping ions in KY_3F_{10} replace the Y^{3+} ones in a single type of sites with a C_{4v} symmetry (24*e* Wyckoff position) [15]. This process is promoted by the closeness of the ionic radii of Tm^{3+} (1.13 Å) and Y^{3+} (1.16 Å) for VIII-fold F^- coordination. The refractive index of KY_3F_{10} is $n \approx 1.49$ [29].

A simplified scheme of energy levels of Tm^{3+} in KY_3F_{10} is shown in Fig. 2(a); the Stark splitting is according to [15]. The total splitting of the ground-state $\Delta E(^3H_6)$ is 484 cm^{-1} and

the zero-phonon-line (ZPL) energy for the $^3F_4 \rightarrow {}^3H_6$ transition is 5777 cm^{-1}. In Fig. 2(b), we show the absorption cross-section, σ_{abs}, for the $^3H_6 \rightarrow {}^3H_4$ transition suitable for diode-pumping. The maximum $\sigma_{abs} = 0.79\times10^{-20}$ cm^2 is at 778.6 nm ($\Gamma_{3,4} \rightarrow \Gamma_5$) and the corresponding full width at half maximum (FWHM) is 2.9 nm. At longer wavelengths, a weaker and broader absorption peak is observed at 802.2 nm ($\sigma_{abs} = 0.22\times10^{-20}$ cm^2 and FWHM = 13.9 nm).

For the $^3H_6 \leftrightarrow {}^3F_4$ transition, Fig. 1(c), the maximum $\sigma_{abs} = 0.82\times10^{-20}$ cm^2 is at 1646.2 nm ($\Gamma_{3,4} \rightarrow \Gamma_5$). The stimulated-emission (SE) cross-section, σ_{SE}, was calculated by a combination of the reciprocity method (RM) [30] using the Stark splitting and the Füchtbauer–Ladenburg (F-L) formula [31] using the radiative lifetime of the emitting state, $\tau_{rad}(^3F_4) = 9.41$ ms [15]. The maximum $\sigma_{SE} = 0.65\times10^{-20}$ cm^2 is at 1846.0 nm ($\Gamma_1 \rightarrow \Gamma_1$). The measured free-of-reabsorption lifetime of the $^3F_4$ state is about 16 ms.

The primitive cell of KY_3F_{10} contains two formula units resulting in 84 degrees of freedom. At the center of the Brillouin zone Γ ($\boldsymbol{k} = 0$), the irreducible representation can be written as follows: $\Gamma = 3A_{1g} + A_{2g} + 2A_{2u} + 4E_g + 2E_u + 4F_{1g} + 8F_{1u} + 6F_{2g} + 4F_{2u}$ of which A_{1g}, E_g and F_{2g} are Raman-active. The unpolarized Raman spectrum of Tm^{3+}:KY_3F_{10} is shown in Fig. 3. The most intense line is at 378 cm^{-1} (E_g) and the maximum phonon energy is 495 cm^{-1} (E_g). For the E_g modes, most of the Y and F atoms move in opposite directions leading to deformative vibrations of the fluorine polyhedra.

3.2 Thermo-optical properties

For the studies of the thermo-optical properties, we used a rectangular sample cut from an undoped KY_3F_{10} boule with a thickness of 7.89 mm and aperture of 3.85×3.47 mm^2. The thermal expansion coefficient of KY_3F_{10} $\alpha = 11.3\pm0.2\times10^{-6}$ K^{-1} was measured using a horizontal dilatometer (Netzsch 402 PC) in the range of temperatures of 20–200 °C. The volumetric thermal expansion is then $\alpha_{vol} = 3\alpha = 33.9\times10^{-6}$ K^{-1}.

The thermo-optic coefficients (TOCs), dn/dT, and thermal coefficients of the optical path (TCOPs), $W = \mathrm{d}n/\mathrm{d}T + (n - 1)\alpha$, were measured using the laser beam deviation method for a medium with a linear thermal gradient [32]. The thermal gradient in the sample was ~10 ºC/mm. The measurements were performed around room temperature (25 ºC) for several wavelengths in the 0.40-1.06 μm spectral range, see Fig. 4. At 633 nm, $\mathrm{d}n/\mathrm{d}T = -9.2\pm0.5\times10^{-6}$ K^{-1} and $W = -3.7\pm0.5\times10^{-6}$ K^{-1}. The negative TCOPs for KY_3F_{10} suggest a negative thermal lens in crystals doped with RE^{3+} ions. The dispersion of both thermo-optic constants is weak.

The wavelength-dependence of the dn/dT coefficients of dielectric crystals can be accounted for by the following model [33]:

$$\mathrm{d}n/\mathrm{d}T = -\alpha_{vol}\frac{(n_\infty^2-1)}{2n(\lambda)}\frac{\lambda^2}{\lambda^2-\lambda_g^2} - \frac{1}{E_g}\frac{\mathrm{d}E_g}{\mathrm{d}T}\frac{(n_\infty^2-1)}{2n(\lambda)}\left(\frac{\lambda^2}{\lambda^2-\lambda_g^2}\right)^2. \quad (1)$$

Here, λ is the light wavelength, n_∞ is the refractive index in the long-wavelength limit, E_g is the electronic bandgap, λ_g is the corresponding wavelength, $\lambda_g(\mu m) = 1.2398/E_g(eV)$, and d$E_g$/d$T$ is the temperature coefficient of the bandgap. This model explains the temperature dependence of the refractive index by a counteraction of the volumetric thermal expansion (leading to a decreased crystal density and thus, a decreased refractive index n via the Clausius-Mossotti

relation) and a temperature dependence of the bandgap (typically leading to an increase of the refractive index because $dE_g/dT < 0$ for most of the dielectric crystals).

For KY_3F_{10}, only the E_g value of ~10 eV [34] was reported. Thus, we fitted the experimental data of the dispersion of the dn/dT coefficients, Fig. 4, using Eq. (1) with dE_g/dT as a free parameter. The best fit dE_g/dT value is $-0.7\pm0.1\times10^{-4}$ eV/K. The calculated thermo-optic dispersion curve $dn/dT(\lambda)$, is nearly constant in the visible and near-IR. This gives an estimation of dn/dT (~1.9 μm) = -8.9×10^{-6} K^{-1}. Physically, negative thermo-optic coefficients in KY_3F_{10} are related to high volumetric thermal expansion for this wide bandgap material.

4. Laser performance

4.1 Laser set-up

The scheme of the compact diode-pumped Tm^{3+}:KY_3F_{10} laser is shown in Fig. 5(a). A rectangular laser crystal sample was prepared with a thickness t of 3.2 mm and aperture of 3.2×5.3 mm^2. Its input and output surfaces were polished to laser quality and remained uncoated. The crystal was mounted in a Cu-holder using In foil for better thermal contact from the 4 lateral sides. The holder was actively cooled by circulating water (temperature: 12 °C). The simple linear laser cavity consisted of a flat pump mirror (PM) coated for high transmission (HT, $T > 99.75\%$) at 0.7–1 μm and high-reflection (HR) at 1.8–2.1 μm, and a set of concave output couplers (OCs) with radius of curvature (RoC) of 50 mm and transmission at the laser wavelength T_{OC} = 1.5%-15%. The crystal was placed at 1 mm separation from the PM. The geometrical cavity length was 49 mm. The crystal was pumped by a fiber-coupled AlGaAs laser diode (LuOcean P-series Lu0808C, fiber core diameter: 200 μm, N.A.: 0.22) delivering up to 13 W of unpolarized output ($M^2 \approx 80$) at 802 nm (emission bandwidth: ~6 nm). The pump was collimated and focused into the crystal through the PM by a lens assembly (1:1 reimaging ratio, focal length f = 30 mm). The pump spot radius at the focus w_P was 100 μm and the confocal parameter $2z_R$ was 1.4 mm. The measured pump absorption was 40%. The crystal was pumped in a single-pass. The calculated radius of the laser mode in the crystal w_L was 70–80 μm, depending on the pump power.

For the thermal lens measurements, the radius of the TEM_{00} laser mode was measured at 15 cm from the OC using the optical knife method. The optical (refractive) power of the thermal lens D (inverse of its focal length) was calculated using the ray transfer matrix formalism.

For passive Q-switching, we used a saturable absorber (SA) based on single-walled carbon nanotubes (SWCNTs) [35]. The SA consisted of a PMMA film (thickness: 300 nm) containing randomly-oriented (spaghetti-like) arc-discharged SWCNTs deposited on a 1.05-mm-thick uncoated quartz substrate [36]. The mean diameter of the SWCNTs was in the 1.5-2.2 nm range, leading to a broad absorption band spanning from 1.6 to 2.2 μm related to the E_{11} fundamental transition of semiconducting nanotubes, Fig. 5(b). The transmission-type SA was inserted into the cavity near the laser crystal and was placed at normal incidence. The calculated radius of the laser mode w_L at the SA was 110±5 μm. The characteristics of the SWCNT-SA were as follows: small-signal transmission T_{SA} = 97.4%, fraction of the saturable losses $\alpha'_S/\alpha'_{SA} = 0.21$ ($\alpha'_{SA} = 1 - T_{SA}$), saturation intensity I_{sat} = 7 MW/cm^2 and recovery time τ_{rec} = 0.25 and 1.16 ps ("fast" and "slow" components, respectively).

A fast (rise time: <100 ps) Ge PIN photodiode (UPD-100-IR1-P, Alphalas) and a 2 GHz Tektronix DPO5204B digital oscilloscope were used to detect and characterize the Q-switched pulses. The laser emission spectra were measured with a compact spectrometer (WaveScan, sensitivity: 1.0-2.6 μm, APE GmbH). The 2D profile of the laser beam was measured with a FIND-R-SCOPE near-IR camera (model 85726).

4.2 Continuous-wave laser

Without the SA in the cavity, the Tm^{3+}:KY_3F_{10} laser operated in the continuous-wave (CW) mode. The laser output was unpolarized. The best laser performance was observed for TOC = 9% with which the laser generated a maximum output power of 1.85 W at ~1891 nm with a maximum slope efficiency η of 65.2% (versus the absorbed pump power P_{abs}), Fig. 6(a). The laser threshold was at P_{abs} = 0.45 W and the optical-to-optical efficiency with respect to the incident pump power η_{opt} was 17.8%. For smaller and higher output coupling, the laser performance deteriorated. For T_{OC} = 15%, the worse laser output is ascribed to upconversion losses related to high inversion. The round-trip passive losses L were estimated from the Caird analysis [37] as 0.5% (passive loss in the crystal: $\delta_{loss} \approx 0.007$ cm^{-1}). No thermal roll-over nor crystal damage were observed up to at least P_{abs} = 3.5 W. The power scaling was limited by the available pump power.

Typical laser emission spectra are shown in Fig. 6(b). The spectra contained multiple peaks due to the broad gain profile of Tm^{3+} in KY_3F_{10} and possible etalon effects at the PM / crystal interface. With the increase of the output coupling, the laser wavelength experienced a blue-shift from 1931-1956 nm (for the smallest T_{OC} = 1.5%) to ~1887 nm (for T_{OC} = 15%). This is due to the quasi-three-level nature of the Tm^{3+} laser scheme exhibiting reabsorption.

In a previous work, a diode-pumped Tm^{3+}:KY_3F_{10} laser generated 0.27 W at 1846 nm with lower η of 42.5% [11]. The observed improvement of the laser performance in the present work is partially due to the higher Tm^{3+} doping level used, promoting the efficiency of the CR mechanism. The CR mechanism is one of the most important factors affecting the slope efficiency of Tm lasers via the pump quantum efficiency η_q [38]:

$$\eta_q = \frac{1/\tau_{30} + 2W_{CR} - (1/\tau_{3rad})(1-\beta_{32})}{1/\tau_{30} + W_{CR}}. \quad (2)$$

Here, τ_{30} and τ_{3rad} are the intrinsic (unquenched, at the limit of low Tm^{3+} concentration) and radiative lifetimes of the pump state ($^3H_4$), respectively, β_{32} = 13.1% is the luminescence branching ratio for the $^3H_4 \rightarrow {}^3F_4 + {}^3H_5$ transitions and W_{CR} is the CR rate (in s^{-1}). For fluoride crystals, and, in particular, for KY_3F_{10}, due to the low energy of the most intense Raman peak $h\nu_{ph}$ = 378 cm^{-1} [39], $\tau_{30} \approx \tau_{3rad}$ = 1.9 ms (otherwise, it may be shortened due to the NR relaxation).

The CR rate for 8 at.% Tm^{3+} doping in KY_3F_{10} is 3.72×10^4 s^{-1}, as estimated from the luminescence lifetimes of the $^3H_4$ state [11]. The corresponding concentration-independent CR parameter $C_{CR} = 0.28\times10^{-37}$ cm^6s^{-1} (where $W_{CR} = C_{CR}\cdot N_{Tm}^2$ [40]). Note that the CR is stronger in Tm^{3+}:KY_3F_{10} as compared to Tm^{3+}:$LiYF_4$ (for the same Tm^{3+} ion density) because of the larger overlap between the emission $^3H_4 \rightarrow {}^3F_4$ and absorption $^3H_6 \rightarrow {}^3F_4$ spectra leading to stronger multipolar interactions between the neighboring Tm^{3+} ions [15]. By using Eq. (2), we

calculated η_q = 1.97. Consequently, the CR in the studied crystal is very efficient explaining the observed high laser efficiency well exceeding the Stokes limit, $\eta_{St} = \lambda_P/\lambda_L$ = 42.4%.

In Table 1, we compare the output characteristics of diode-pumped Tm lasers based on fluoride crystals reported recently. Tm^{3+}-doped fluoride crystals belonging to different classes were studied, namely, monoclinic ($BaLn_2F_8$ for Ln = Y and Y/Lu) [9,41], tetragonal ($LiLnF_4$ for Ln = Y, Gd, Lu) [8,42], trigonal (KYF_4) [43] and cubic (CaF_2, SrF_2) [3,5,44,45]. Note that here, we focus particularly on results achieved using the diode-end-pumping geometry. High-power Tm:$LiYF_4$ lasers delivering tens of watts and based on slab or rod geometries are known [46]. From Table 1, it is concluded that Tm^{3+}:KY_3F_{10} offers good power scaling capabilities and high laser slope efficiency as compared to the most used fluoride crystals (Tm^{3+}:CaF_2, Tm^{3+}:SrF_2). In part, this is related to a higher available Tm^{3+} doping concentration leading to a very efficient CR mechanism.

4.3 Thermal lensing

We have considered the thermal lens as an ideal thin spherical lens located in the center of the Tm^{3+}:KY_3F_{10} crystal. For the studied hemispherical cavity, a positive (focusing, $D > 0$) thermal lens would result in a confinement of the output laser beam, and a negative (defocusing, $D < 0$) one would provide the opposite effect of beam expansion. The latter was observed in our experiment, Fig. 7(a). Thus, a negative thermal lens occurs in Tm^{3+}:KY_3F_{10}. This agrees well with the negative sign of the TCOP coefficient for this crystal, Fig. 4.

Following the ray transfer matrix formalism, we have calculated the optical power of the thermal lens D, Fig. 7(b). The optical power shows almost linear dependence on the absorbed pump power as expressed by the so-called sensitivity factor, $M = dD/dP_{abs} = -10.5\pm0.2$ m^{-1}/W. This parameter shows the variation of the optical power due to 1 W variation of P_{abs}.

For longitudinally diode-pumped crystals (with a "top-hat" pump beam), the sensitivity factor of the thermal lens can be calculated according to [47]:

$$M = \frac{\eta_h}{2\pi w_P^2 \kappa}\chi, \quad \chi = dn/dT + P_{PE} + (1+\nu)(n-1)\alpha. \tag{3}$$

Here, $\kappa \approx 2.5$ W/(m·K) [48] is the thermal conductivity of doped KY_3F_{10}, $\eta_h = P_{heat}/P_{abs} \approx 0.4$ [46] is the fractional heat loading and χ is the "generalized" thermo-optic coefficient (TOC) representing three contributions to the thermal lensing in diode-pumped crystals, namely temperature dependence of the refractive index (expressed by dn/dT), the thermo-optic effect (expressed by the P_{PE} term) and the end-face bulging due to non-uniform thermal expansion (expressed by the $(1 + \nu)(n - 1)\alpha$ term, where ν is the Poisson ratio). Using Eq. (3), we have estimated the "generalized" TOC for Tm^{3+}:KY_3F_{10} crystal as -4.1×10^{-6} K^{-1} at ~1.9 μm which agrees with the experimental TCOP value, Fig. 4.

4.4 Passively Q-switched laser

For passive Q-switching, we studied different OCs. The one with T_{OC} = 9% provided better output power and stability of the PQS operation. The input-output dependence of the PQS laser is shown in Fig. 6(a). The PQS Tm^{3+}:KY_3F_{10} laser generated a maximum average output power of 0.77 W at 1884 nm with η = 34.1%. The laser threshold was at P_{abs} = 0.75 W

and the Q-switching conversion efficiency with respect to the CW laser regime η_{conv} was 41.6% indicating a moderate insertion loss of the SWCNT-SA. The range of pump powers for stable Q-switching had a lower limit due to laser instabilities near the threshold and an upper limit related to excessive heating of the SA by the residual (non-absorbed) pump [49]. The emission wavelength for the PQS laser was slightly shorter compared to CW operation (for the same OC) due to an additional loss introduced by the SA and thus, higher inversion level for the Tm^{3+} ions. During the PQS laser operation, no damage of the crystal or the SA was observed.

The pulse characteristics of the PQS laser are shown in Fig. 8. The pulse duration (FWHM) $\Delta\tau$ and the pulse repetition frequency (PRF) were determined directly, and the pulse energy and peak power were calculated as $E_{out} = P_{out}/PRF$ and $P_{peak} = E_{out}/\Delta\tau$. For the SWCNT-SA, the recovery time of its initial absorption τ_{rec} is much shorter than the characteristic time of formation of the Q-switched pulses (hundreds of ns), so that it can be classified as a "fast" SA. For lasers PQS by "fast" SAs, the pulse characteristics are dependent on the pump power due to the dynamic bleaching of the SA (increase of the intracavity laser intensity) [50]. This is also observed in Fig. 8. The pulse duration decreased from 625 to 490 ns while the PRF increased almost linearly from 17 to 58 kHz and E_{out} increased from 5.9 to 13.2 μJ. The peak power reached 26.9 W. The calculated spatially averaged intracavity laser intensity on the SA I_{in} was ~2 MW/cm^2. Thus, the SA was partially saturated.

A typical oscilloscope trace of the single Q-switched pulse and the corresponding pulse train are shown in Fig. 9 (measured at the pump power equal to the upper limit of the Q-switching stability). The intensity instabilities in the pulse train are relatively high (20%) due to the effect of the residual pump heating the SA.

In Table 2, we compared the pulse characteristics of bulk ~2 μm lasers PQS by SWCNTs reported so far [36,51-56]. In previous studies, only oxide crystals and ceramics doped with Tm^{3+} and Ho^{3+} ions were implemented. The energy storage capabilities of these materials in PQS lasers are limited due to the shorter lifetimes of their upper laser levels as compared to fluorides. In [36], a Tm^{3+}:$KLu(WO_4)_2$ laser PQS by a similar SWCNT-SA as in the present work, provided a pulse energy of only 4.0 μJ (compare to 13.2 μJ for Tm^{3+}:KY_3F_{10}). In [51,54], similar pulse energies were achieved by employing SWCNT-SAs with much higher modulation depths ($\alpha'_{SA} \approx 14\%$). We conclude, that Tm^{3+}:KY_3F_{10} is very promising for PQS laser applications.

5. Conclusions

To conclude, we have revisited the spectroscopic, thermo-optical and laser properties of the cubic KY_3F_{10} fluoride crystal doped with Tm^{3+} ions. As compared to the widespread cubic fluorite-type crystals (CaF_2, SrF_2), Tm^{3+}:KY_3F_{10} shows a lower growth temperature and higher available Tm^{3+} doping levels (8 at.%, as studied in the present work) while preserving good optical quality. Despite the moderate thermal conductivity of KY_3F_{10}, it possesses a negative thermo-optic coefficient, dn/dT, leading to partial "athermal" compensation of different effects contributing to the formation of the thermal lens. Moreover, Tm^{3+}:KY_3F_{10} is characterized by an efficient cross-relaxation mechanism for the adjacent Tm^{3+} ions leading to a high laser slope efficiency (up to 65%, as achieved in the present work) under pumping with AlGaAs laser

diodes. Finally, the long upper laser level lifetime of Tm^{3+} in KY_3F_{10} leads to good energy storage capabilities in PQS lasers as demonstrated in the present work with a SWCNT-based "fast" SA.

Further work on Tm^{3+}:KY_3F_{10} should focus on the growth of crystals with even higher doping levels (up to 18 at.% Tm^{3+}, as attempted in our preliminary experiments) resulting in both high pump absorption efficiency and strong CR leading to efficient laser operation. Under such conditions, the so-called "vibronic" laser operation potentially leading to laser emission at >2 μm is expected. PQS Tm^{3+}:KY_3F_{10} lasers by "slow" SAs, such as Cr^{2+}:ZnS or Cr^{2+}:ZnSe, may produce mJ-energy level pulses at low repetition rates (few kHz).

Acknowledgments

This work was supported by Spanish Government (projects No. MAT2016-75716-C2-1-R (AEI/FEDER,UE); Generalitat de Catalunya (project No. 2017SGR755). National Science Foundation (NSF) (projects No. 11704155, 61475067, 61605062, 61735005); National Key Research and Development Program of China (project No. 2017YFB1104500). P. L. acknowledges financial support from the Government of the Russian Federation (Grant 074-U01) through ITMO Post-Doctoral Fellowship scheme. P. L. would like to thank Dr. Christian Kränkel (Zentrum für Lasermaterialien, Leibniz-Institut für Kristallzüchtung, Berlin) for providing a KY_3F_{10} sample for the thermo-optic studies.

References

[1] A. A. Kaminskii, Laser crystals: Their physics and properties (Springer, 2013).

[2] B. M. Walsh, N. P. Barnes, B. Di Bartolo, Branching ratios, cross sections, and radiative lifetimes of rare earth ions in solids: Application to Tm^{3+} and Ho^{3+} ions in $LiYF_4$, J. Appl. Phys. 3 (1998) 2772–2787.

[3] P. Camy, J. L. Doualan, S. Renard, A. Braud, V. Menard, R. Moncorgé, Tm^{3+}:CaF_2 for 1.9 μm laser operation, Opt. Commun. 236 (2004) 395-402.

[4] G. Brasse, P. Loiko, C. Grygiel, P. Leprince, A. Benayad, F. Lemarie, J.-L. Doualan, A. Braud, P. Camy, Liquid Phase Epitaxy growth of Tm^{3+}-doped CaF_2 thin-films based on LiF solvent, J. Alloys Compd. 803 (2019) 442-449.

[5] A. Sottile, E. Damiano, M. Rabe, R. Bertram, D. Klimm, M. Tonelli, Widely tunable, efficient 2 μm laser in monocrystalline Tm^{3+}:SrF_2, Opt. Express 26 (2018) 5368-5380.

[6] Z. Zhou, B. Mei, J. Song, W. Li, Y. Yang, G. Yi, Effects of Sr^{2+} content on microstructure and spectroscopic properties of Nd^{3+} doped $Ca_{1-x}Sr_xF_2$ transparent ceramics, J. Alloys Compd. 811 (2019) 152046.

[7] G. Galzerano, E. Sani, A. Toncelli, G. Della Valle, S. Taccheo, M. Tonelli, P. Laporta, Widely tunable continuous-wave diode-pumped 2-μm Tm–Ho:KYF_4 laser, Opt. Lett. 29 (2004) 715-717.

[8] P. Loiko, J. M. Serres, X. Mateos, S. Tacchini, M. Tonelli, S. Veronesi, D. Parisi, A. Di Lieto, K. Yumashev, U. Griebner, V. Petrov, Comparative spectroscopic and thermo-optic study of Tm:$LiLnF_4$ (Ln = Y, Gd, and Lu) crystals for highly-efficient microchip lasers at ~2 μm, Opt. Mater. Express 7 (2017) 844-854.

[9] F. Cornacchia, D. Parisi, C. Bernardini, A. Toncelli, M. Tonelli, Efficient, diode-pumped Tm^{3+}:BaY_2F_8 vibronic laser, Opt. Express 12 (2004) 1982-1989.

[10] X. Wang, Y. Hou, J. Qu, J. Ding, H. Lin, L. Liu, Y. Zhou, F. Zeng, C. Li, Z. Su, Up-conversion photoluminescence properties and energy transfer process of Ho^{3+},Yb^{3+} co-doped BaY_2F_8 fine fibers, J. Alloys Compd. 212 (2019) 145-159.

[11] A. Braud, P. Tigreat, J. Doualan, R. Moncorgé, Spectroscopy and cw operation of a 1.85 μm Tm:KY_3F_{10} laser," Appl. Phys. B 72 (2001) 909-912.

[12] P. Camy, J. L. Doualan, R. Moncorgé, J. Bengoechea, U. Weichmann, Diode-pumped Pr^{3+}:KY_3F_{10} red laser, Opt. Lett. 32 (2007) 1462-1464).

[13] M. Schellhorn, D. Parisi, S. Veronesi, G. Bolognesi, M. Eichhorn, M. Tonelli, In-band pumped Ho^{3+}:KY_3F_{10} 2 μm laser, Opt. Lett. 38 (2013) 504-506.

[14] P. A. Loiko, E. V. Vilejshikova, N. M. Khaidukov, M. N. Brekhovskikh, X. Mateos, M. Aguiló, K. V. Yumashev, Judd–Ofelt modeling, stimulated-emission cross-sections and non-radiative relaxation in Er:K_2YF_5 crystals, J. Lumin. 180 (2016) 103-110.

[15] M. Diaf, A. Braud, C. Labbé, J. L. Doualan, S. Girard, J. Margerie, R. Moncorgé, M. Thuau, Synthesis and spectroscopic studies of Tm^{3+}-doped KY_3F_{10} single crystals, Canad. J. Phys. 77 (2000) 693-697.

[16] K. Friese, H. Krüger, V. Kahlenberg, T. Balić-Zunić, H. Emerich, J. Y. Gesland, A. Grzechnik, Study of the temperature dependence of the structure of KY_3F_{10}, J. Phys.: Cond. Matter 18 (2006) 2677-2687.

[17] P. Loiko, P. Koopmann, X. Mateos, J. M. Serres, V. Jambunathan, A. Lucianetti, T. Mocek, M. Aguiló, F. Díaz, U. Griebner, V. Petrov, C. Kränkel, Highly-efficient, compact Tm^{3+}:RE_2O_3 (RE = Y, Lu, Sc) sesquioxide lasers based on thermal guiding, IEEE J. Sel. Top. Quantum Electron. 24 (2018) 1600713-1-13.

[18] P. Loiko, L. Zhang, J.M. Serres, Y. Wang, M. Aguiló, F. Díaz, Z. Lin, H. Lin, G. Zhang, E. Vilejshikova, E. Dunina, A. Kornienko, L. Fomicheva, V. Petrov, U. Griebner, W. Chen, and X. Mateos, "Monoclinic Tm:$MgWO_4$ crystal: Crystal-field analysis, tunable and vibronic laser demonstration," J. Alloy Compd 763 (2018) 581-591.

[19] K. Scholle, S. Lamrini, P. Koopmann, P. Fuhrberg, 2 μm laser sources and their possible applications, in Frontiers in Guided Wave Optics and Optoelectronics, B. Pal, Ed. (InTech, 2010), pp. 471–500.

[20] R. C. Stoneman, L. Esterowitz, Efficient, broadly tunable, laser-pumped Tm:YAG and Tm:YSGG cw lasers, Opt. Lett. 15 (1990) 486-488.

[21] A. Braud, S. Girard, J. L. Doualan, M. Thuau, R. Moncorgé, A. M. Tkachuk, Energy-transfer processes in Yb:Tm-doped KY_3F_{10}, $LiYF_4$, and BaY_2F_8 single crystals for laser operation at 1.5 and 2.3 μm, Phys. Rev. B 61 (2000) 5280-5292.

[22] A. Muti, M. Tonelli, V. Petrov, and A. Sennaroglu, Continuous-wave mid-infrared laser operation of Tm^{3+}:KY_3F_{10} at 2.3 μm, Opt. Lett. 44 (2019) 3242-3245.

[23] Y. V. Orlovskii, A. V. Popov, E. O. Orlovskaya, A. S.Vanetsev, E. A. Vagapova, M. Rähn, V. Sammelselg, I. Sildos, A. E. Baranchikov, P. V. Grachev, V. B. Loschenov, A. V. Ryabova, Comparison of concentration dependence of relative fluorescence quantum yield and brightness in first biological window of wavelengths for aqueous colloidal

solutions of Nd^{3+}:LaF_3 and Nd^{3+}:KY_3F_{10} nanocrystals synthesized by microwave-hydrothermal treatment, J. Alloys Compd. 6 (2018)182-192.
[24] T. Pang, R. Jian, J. Xie, W. Lu, Up-conversion luminescence and photo-thermal effect of KY_3F_{10}:Yb^{3+},Ho^{3+} nanocrystals, J. Phys. D: Appl. Phys. 51 (2018) 355301.
[25] R. U. Ichikawa, H. S. M. D. Linhares, I. Peral, S. L. Baldochi, I. M. Ranieri, X. Turrillas, L. G. Martinez, Evidence for a core–shell configuration in Tb-doped KY_3F_{10} nanoparticles using synchrotron x-ray line profile and pair distribution function analyses, Mater. Res. Express 5 (2018) 015006.
[26] N. G. Debelo, F. B. Dejene, K. Roro, T. Senbeta, B. Mesfin, T. Abebe, L. Mostert, Enhanced emission and improved crystallinity of KY_3F_{10}:Ho^{3+} thin films grown at high deposition temperature using pulsed laser deposition technique," J. Electron. Mater. 47 (2018) 2617-2624.
[27] Y. Peng, D. Chen, J. Zhong, X. Li, Q. Mao, F. Chi, Lanthanide-doped KGd_3F_{10} nanocrystals embedded glass ceramics: Self-crystallization, optical properties and temperature sensing, J. Alloys Compd. 767 (2018) 682-689.
[28] D. Parisi, S. Veronesi, M. Tonelli, A method of bulk crystals formation, in particular single crystals of fluorides doped with rare earth ions, patent IT TO2011A000335 (2011).
[29] P. Porcher, P. Caro, Crystal field parameters for Eu^{3+} in KY_3F_{10}. III. Radiative and nonradiative transition probabilities, J. Chem. Phys. 68 (1978) 4183-4187.
[30] S. A. Payne, L. L. Chase, L. K. Smith, W. L. Kway, W. F. Krupke, Infrared cross-section measurements for crystals doped with Er^{3+}, Tm^{3+}, and Ho^{3+}, IEEE J. Quantum Electron. 28 (1992) 2619-2630.
[31] B. Aull, H. Jenssen, Vibronic interactions in Nd:YAG resulting in nonreciprocity of absorption and stimulated emission cross sections, IEEE J. Quantum Electron. 18 (1982) 925-930.
[32] P. Loiko, F. Druon, P. Georges, B. Viana, K. Yumashev, Thermo-optic characterization of Yb:$CaGdAlO_4$ laser crystal, Opt. Mater. Express 4 (2014) 2241-2249.
[33] P. A. Loiko, K. V. Yumashev, N. V. Kuleshov, G. E. Rachkovskaya, A. A. Pavlyuk, Thermo-optic dispersion formulas for monoclinic double tungstates $KRe(WO_4)_2$ where Re = Gd, Y, Lu, Yb, Opt. Mater. 33 (2011) 1688-1694.
[34] N. G. Debelo, F. B. Dejene, K. T. Roro, Pulsed laser deposited KY_3F_{10}:Ho^{3+} thin films: Influence of target to substrate distance, Mater. Chem. Phys. 190 (2017) 62-67.
[35] W. B. Cho, J. H. Yim, S. Y. Choi, S. Lee, A. Schmidt, G. Steinmeyer, U. Griebner, V. Petrov, D.-I. Yeom, K. Kim, F. Rotermund, Boosting the nonlinear optical response of carbon nanotube saturable absorbers for broadband mode-locking of bulk lasers, Adv. Funct. Mater. 20 (2010) 1937–1943.
[36] P. Loiko, X. Mateos, S. Y. Choi, F. Rottermund, J. M. Serres, M. Aguiló, F. Díaz, K. Yumashev, U. Griebner, V. Petrov, Vibronic thulium laser at 2131 nm Q-switched by single-walled carbon nanotubes, J. Opt. Soc. Am. B. 33 (2016) D19-D27.
[37] J. A. Caird, S. A. Payne, P. R. Staber, A. J. Ramponi, L. L. Chase, W. F. Krupke, Quantum electronic properties of the $Na_3Ga_2Li_3F_{12}$:Cr^{3+} laser, IEEE J. Quantum Electron. 24 (1988) 1077–1099.

[38] E. C. Honea, R. J. Beach, S. B. Sutton, J. A. Speth, S. C. Mitchell, J. A. Skidmore, M. A. Emanuel, S. A. Payne, 115-W Tm: YAG diode-pumped solid-state laser, IEEE J. Quantum Electron. 33 (1997) 1592-1600.

[39] M. Mortier, J. Y. Gesland, M. Rousseau, M. A. Pimenta, L. O. Ladeira, J. M. Da Silva, G. A.Barbosa, Raman scattering investigations of KY_3F_{10}, J. Raman Spectr. 22 (1991) 393-396.

[40] P. Loiko M. Pollnau, Stochastic model of energy-transfer processes among rare-earth ions. Example of $Al_2O_3:Tm^{3+}$, J. Phys. Chem. C 120 (2016) 26480-26489.

[41] D. Parisi, S. Veronesi, A. Volpi, M. Gemmi, M. Tonelli, A. Cassanho, H. P. Jenssen, Spectroscopy and laser test emission in Tm^{3+}: $BaYLuF_8$ single crystal, J. Phys. D: Appl. Phys. 47 (2014) 025101-1-7.

[42] F. Cornacchia, A. Di Lieto, M. Tonelli, $LiGdF_4:Tm^{3+}$: spectroscopy and diode-pumped laser experiments, Appl. Phys. B 96 (2009) 363-368.

[43] F. Cornacchia, D. Parisi, E. Sani, A. Toncelli, M. Tonelli, Comparative analysis of the 2 μm emission in $Tm^{3+}:BaY_2F_8$ and $Tm^{3+}:KYF_4$: spectroscopy and laser experiment, in Advanced Solid-State Photonics (OSA, 2005), paper WB23.

[44] C. Zhang, J. Liu, X. Fan, Q. Peng, X. Guo, D. Jiang, X. Qian, L. Su, Compact passive Q-switching of a diode-pumped Tm,Y:CaF_2 laser near 2 μm, Opt. Laser Technol. 103 (2018) 89-92.

[45] Z. Zhang, X. Guo, J. Wang, C. Zhang, J. Liu, L. Su, High-efficiency 2 μm continuous-wave laser in laser diode-pumped Tm^{3+}, $La^{3+}:CaF_2$ single crystal, Opt. Lett. 43 (2018) 4300-4303.

[46] M. Schellhorn, High-power diode-pumped Tm:YLF laser, Appl. Phys. B 91 (2008) 71–74.

[47] S. Chénais, F. Druon, S. Forget, F. Balembois, P. Georges, On thermal effects in solid-state lasers: the case of ytterbium-doped materials, Prog. Quantum Electron. 30 (2006) 89–153.

[48] P. A. Popov, P. P. Fedorov, V. V. Semashko, S. L. Korableva, M. A. Marisov, E. Y. Gordeev, V. M. Reiterov, V. V. Osiko, Thermal conductivity of crystals formed by fluoritelike phases in $MF-RF_3$ systems (M= Li, Na, and K, R = Rare Earth), Dokl. Phys. 54 (2009) 221-224.

[49] J. M. Serres, P. Loiko, X. Mateos, K. Yumashev, U. Griebner, V. Petrov, M. Aguiló, and F. Díaz, Tm:$KLu(WO_4)_2$ microchip laser Q-switched by a graphene-based saturable absorber, Opt. Express 23 (2015) 14108–14113.

[50] A. S. Yasukevich, P. Loiko, N.V. Gusakova, J.M. Serres, X. Mateos, K.V. Yumashev, N.V. Kuleshov, V. Petrov, U. Griebner, M. Aguiló, F. Díaz, Modeling of graphene Q-switched Tm lasers, Opt. Commun. 389 (2017) 15-22.

[51] T. Feng, K. Yang, S. Zhao, J. Zhao, W. Qiao, T. Li, L. Zheng, J. Xu, Q. Wang, X. Xu, L. Su, Efficient CW dual-wavelength and passively Q-switched Tm:LuAG lasers, IEEE Photon. Technol. Lett. 27 (2015) 7-10.

[52] Y. Li, J. Liu, H. Zhu, L. Zheng, L. Su, J. Xu, Y. Wang, Performance of diode-pumped Tm^{3+}:Sc_2SiO_5 crystal passively Q-switched 2 μm laser, Opt. Commun. 330 (2014) 151-154.

[53] X. Xu, Z. Hu, D. Li, P. Liu, J. Zhang, B. Xu, J. Xu, First laser oscillation of diode-pumped Tm^{3+}-doped $LuScO_3$ mixed sesquioxide ceramic, Opt. Express 25 (2017) 15322-15329.

[54] Z. Qu, Y. Wang, J. Liu, L. Zheng, L. Su, J. Xu, Performance of 2 μm Tm:YAP pulse laser based on a carbon nanotube absorber, Appl. Phys. B 109 (2012) 143-147.

[55] T. L. Feng, S. Z. Zhao, K. J. Yang, G. Q. Li, D. C. Li, J. Zhao, W. C. Qiao, L. H. Zheng, J. Xu, G. J. Zhao, Y. G. Wang, A diode-pumped passively Q-switched Tm, Ho:YAP laser with a single-walled carbon nanotube, Laser Phys. Lett. 10 (2013) 095001.

[56] R. Lan, P. Loiko, X. Mateos, Y. Wang, J. Li, Y. Pan, S. Y. Choi, M. H. Kim, F. Rotermund, A. Yasukevich, K. Yumashev, U. Griebner, V. Petrov, Passive Q-switching of microchip lasers based on Ho:YAG ceramic, Appl. Opt. 55 (2016) 4877–4887.

Figure captions

Fig. 1. Photograph of the as-grown high-quality 8 at.% Tm^{3+}:KY_3F_{10} crystal boule.

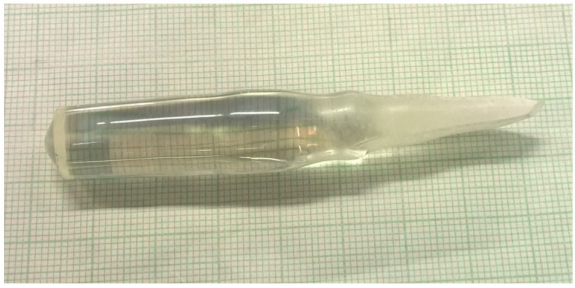

Fig. 2. Spectroscopy of Tm^{3+} ions in cubic KY_3F_{10} crystal: (a) simplified scheme of energy levels: *blue* and *red arrows* - pump and laser transitions, respectively, CR – cross-relaxation, NR – non-radiative decay, the Stark splitting is according to [15]; (b) absorption cross-section, σ_{abs}, for the $^3H_6 \rightarrow {}^3H_4$ transition, *blue arrow* – pump wavelength; (c) absorption, σ_{abs}, and stimulated-emission (SE), σ_{SE}, cross-sections for the $^3H_6 \leftrightarrow {}^3F_4$ transition, *red arrow* – laser wavelength.

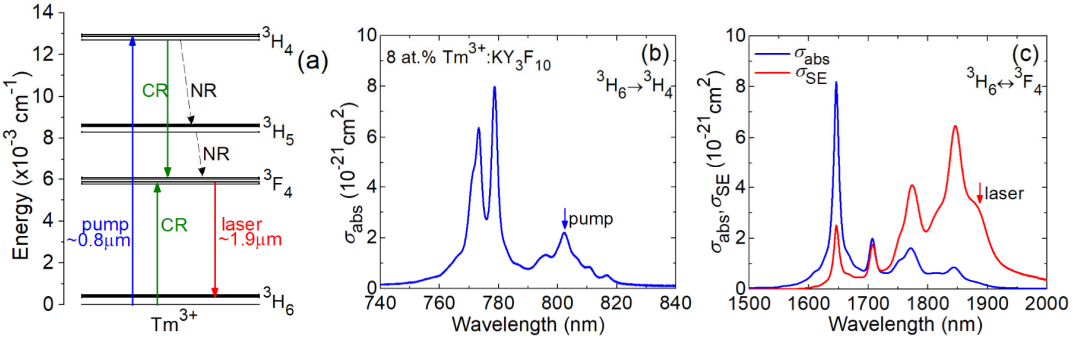

Fig. 3. Unpolarized Raman spectrum of the 8 at.% Tm^{3+}:KY_3F_{10} crystal. *Numbers* denote the energies of the Raman peaks in cm^{-1}. The excitation wavelength is 514 nm.

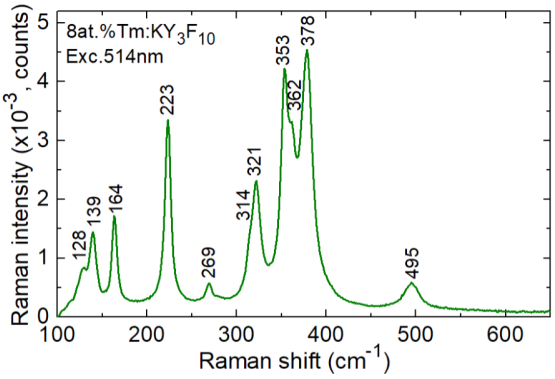

Fig. 4. Dispersion of the thermo-optic coefficient (TOCs), dn/dT, and thermal coefficient of the optical path (TCOP), W = dn/dT + (n – 1)α, for KY_3F_{10}: *symbols* – experimental data, *curves* – modeling with Eq. (1).

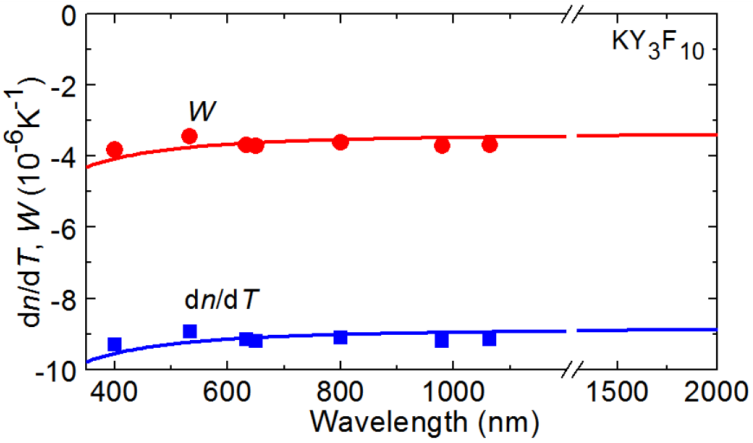

Fig. 5. (a) Scheme of the laser set-up: LD – laser diode, PM – pump mirror, OC – output coupler, SA – saturable absorber; (b) Small-signal transmission spectrum of the SWCNT-SA (Fresnel losses from the quartz substrate are subtracted).

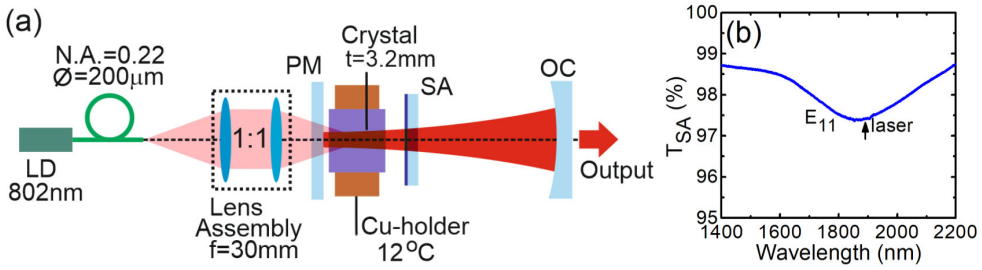

Fig. 6. Diode-pumped continuous-wave and SWCNT passively Q-switched Tm:KY_3F_{10} lasers: (a) input-output dependences, η – slope efficiency; (b) typical laser emission spectra, measured at P_{abs} = 3.1 W.

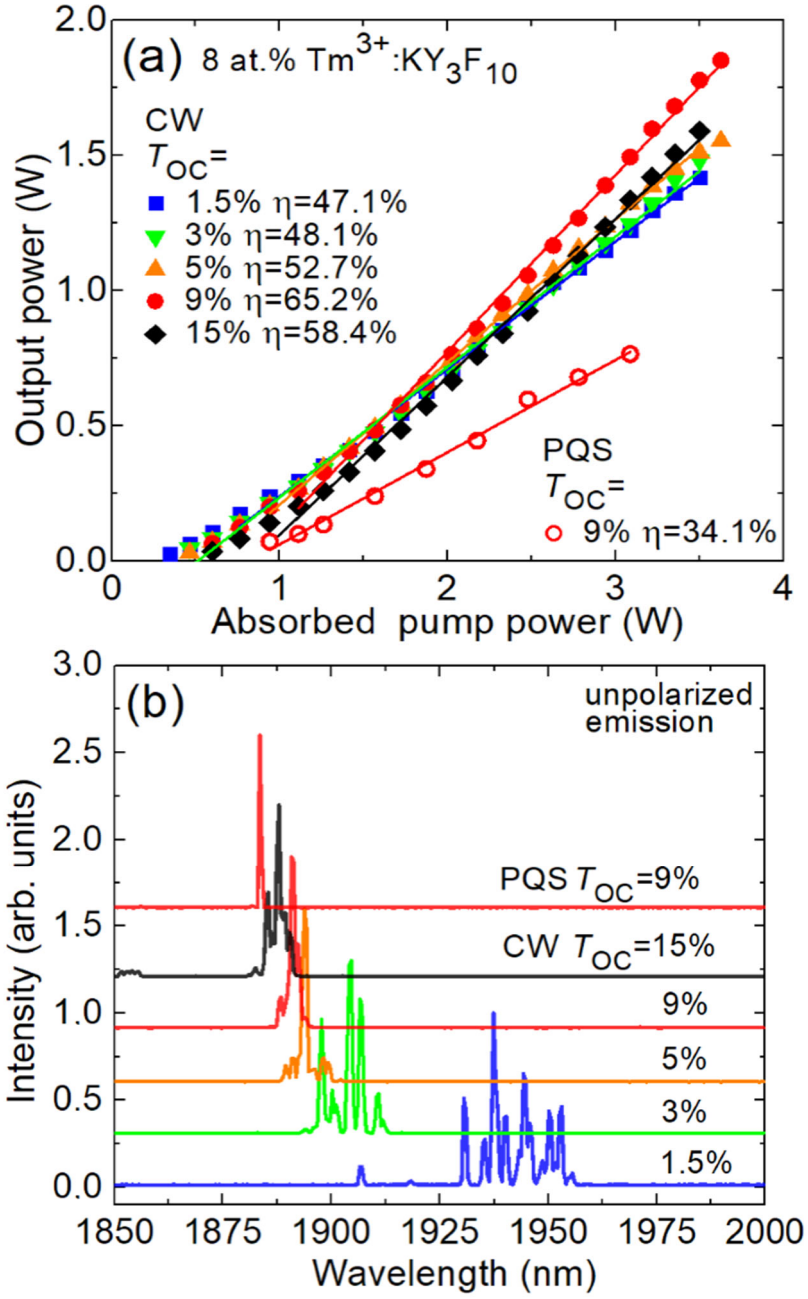

Fig. 7. Evaluation of the thermal lensing in diode-pumped Tm^{3+}:KY_3F_{10}: (a) radius of the laser mode (*circles* – experimental data, *red curve* – calculation based on ray transfer matrix formalism, *inset* – typical 2D profile of the laser mode), measured at 15 cm from the OC, T_{OC} = 9%; (b) optical power of the thermal lens D, *red line* – linear fit for the calculation of the thermal lens sensitivity factor (M).

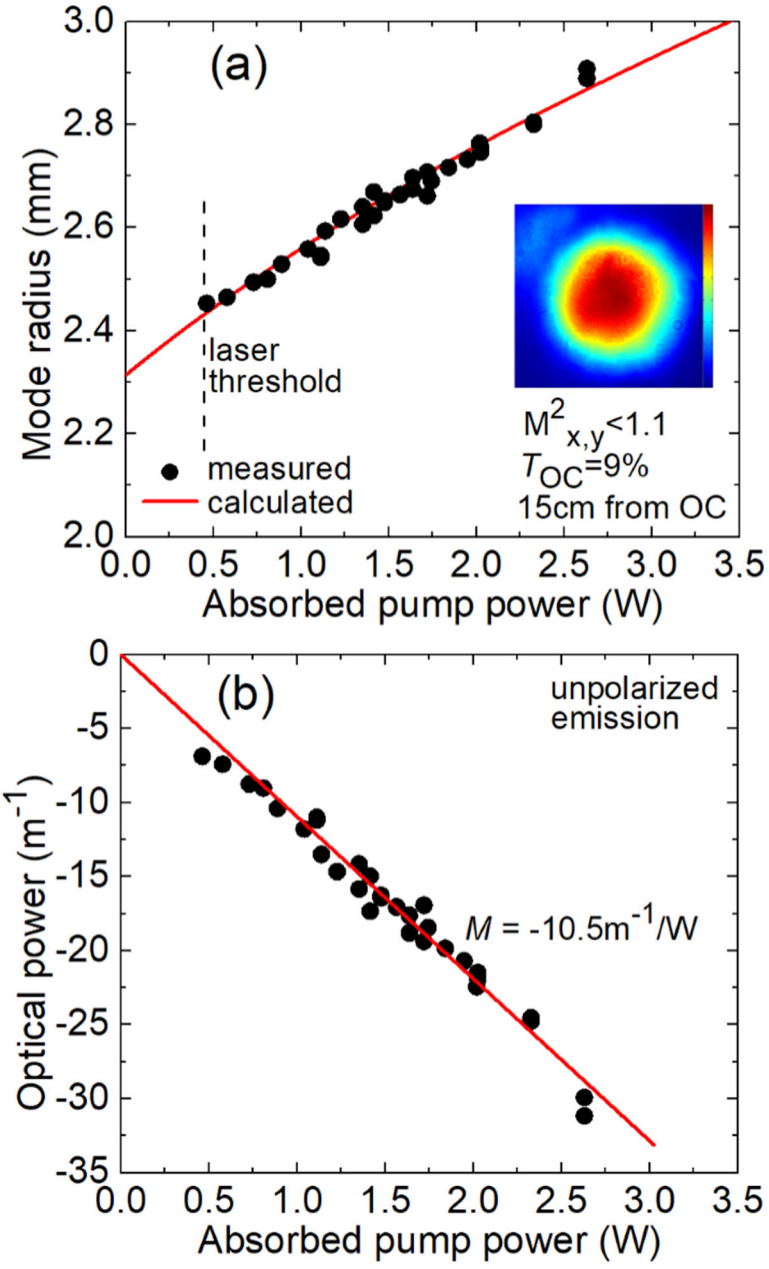

Fig. 8. SWCNT-SA passively Q-switched Tm^{3+}:KY_3F_{10} laser: (a) pulse duration (FWHM) and pulse repetition frequency (PRF), (b) pulse energy and peak power. T_{OC} = 9%.

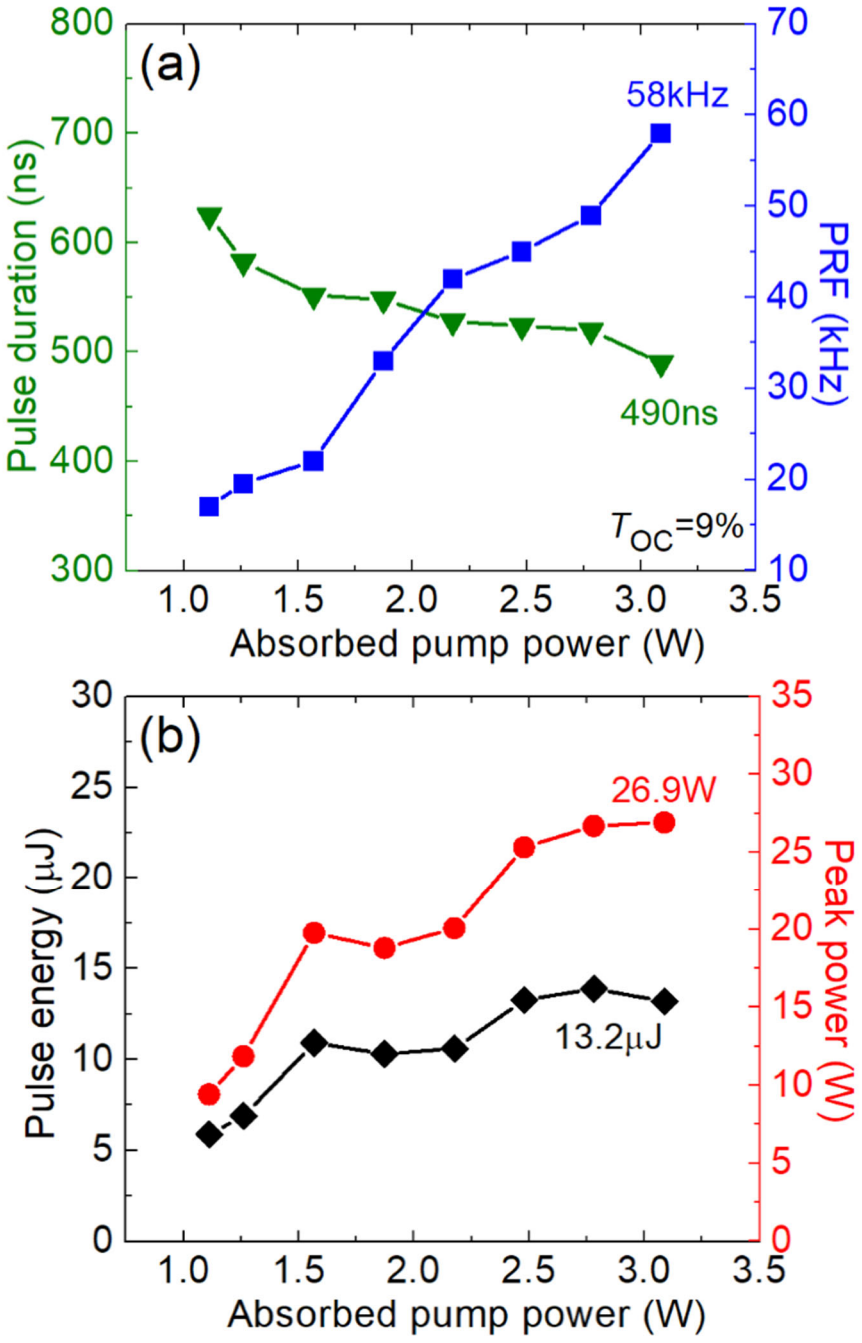

Fig. 9. Oscilloscope traces of the single Q-switched pulse (a) and the pulse train (b) from the SWCNT-SA passively Q-switched Tm^{3+}:KY_3F_{10} laser, T_{OC} = 9%, P_{abs} = 3.1 W.

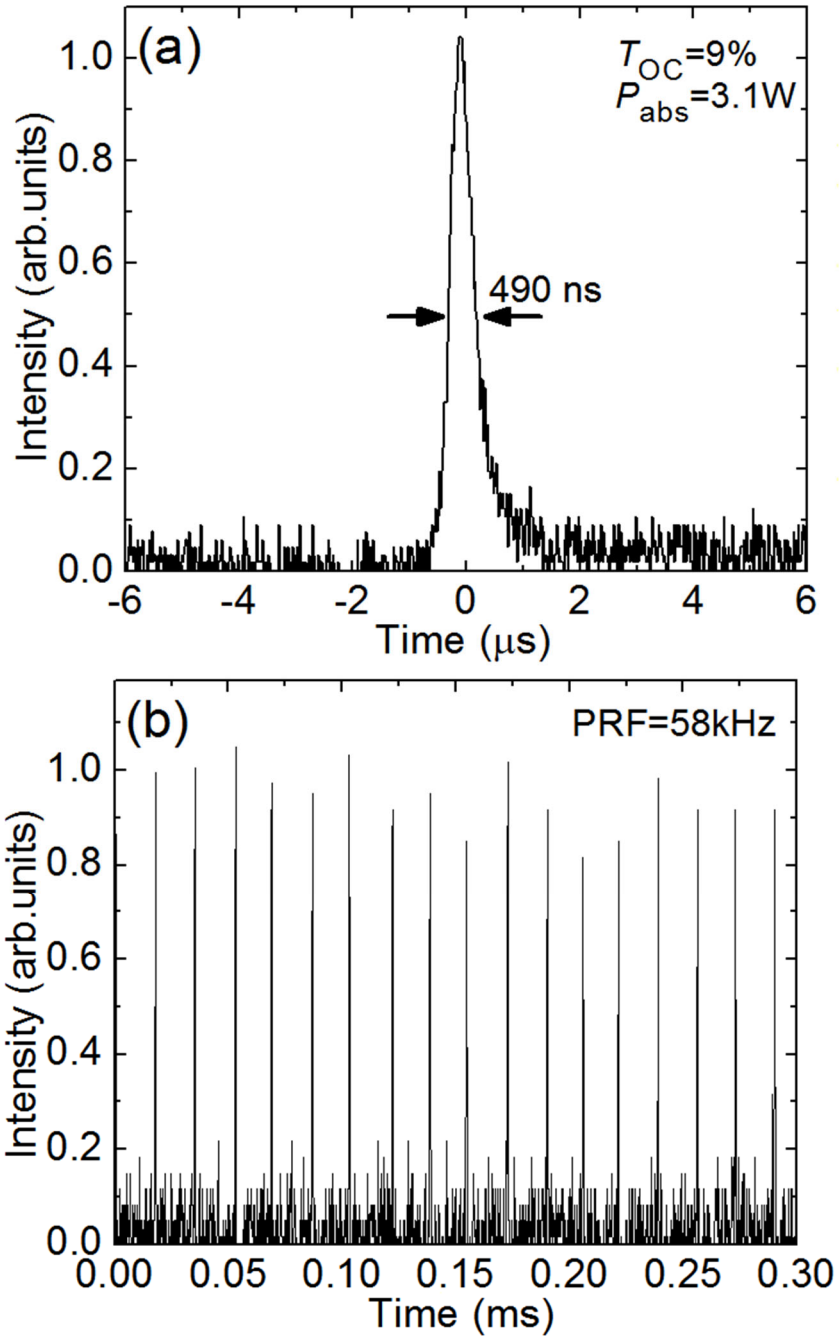

Table 1. Output characteristics* of diode-pumped thulium fluoride crystalline lasers reported recently.

Crystal	Doping	P_{out}, W	P_{th}, W	η, %	λ_L, nm	Polariz.	Ref.
Tm:BaY_2F_8	12 at.%	0.29	0.03	61	1978-2030	unpolar.	[9]
Tm:$BaYLuF_8$	12 at.%	0.11	0.09	27.7	~1920	linear	[41]
Tm:$LiYF_4$	8 at.%	3.10	0.24	72	1904	linear	[8]
Tm:$LiLuF_4$	12 at.%	2.65	0.46	52	1916	linear	[8]
Tm:$LiGdF_4$	12 at.%	0.21	0.04	53	1990-2018	linear	[42]
Tm:KYF_4	10 at.%	0.17	0.05	34	2010-2022	linear	[43]
Tm:CaF_2	1.3 at.%	0.14	0.07	41	1887	unpolar.	[3]
Tm,Y:CaF_2	4 at.%	1.01	0.25	51.5	1972	unpolar.	[44]
Tm,La:CaF_2	3 at.%	4.27	0.37	67.8	1921	unpolar.	[45]
Tm:SrF_2	5.2 at.%	0.53	0.33	43	2025	unpolar.	[5]
Tm:KY_3F_{10}	8 at.%	1.85	0.45	65.2	1891	unpolar.	**

*P_{out} – output power, P_{th} – laser threshold, η – slope efficiency, λ_L – laser wavelength.
**This work.

Table 2. Output characteristics* of ~2 μm lasers passively Q-switched by SWCNTs reported so far.

Material	P_{out}, W	η, %	λ_L, nm	E_{out}, μJ	$\Delta\tau$, ns	PRF, kHz	Ref.
Tm:$KLu(WO_4)_2$	0.99	40	1919	4.0	40	246	[36]
Tm:$Lu_3Al_5O_{12}$	1.55	32.4	2022	17.6	405	88.2	[51]
Tm:Sc_2SiO_5	0.19	~6	1970	3.4	442	55.6	[52]
Tm:$LuScO_3$	0.03	~2	1976	0.95	590	34.7	[53]
Tm:$YAlO_3$	0.30	~8	2010	13.6	255	21.8	[54]
Tm:KY_3F_{10}	0.77	34.1	1884	13.2	490	58	**
Tm,Ho:$YAlO_3$	0.66	14.7	2131	2.7	135	245	[55]
Ho:$Y_3Al_5O_{12}$	0.81	68	2090	4.9	85	165	[56]

*P_{out} – average output power, η – slope efficiency, λ_L – laser wavelength, E_{out} – pulse energy, $\Delta\tau$ – pulse duration, PRF – pulse repetition frequency.
**This work.